

www.acsaem.org Article

# Characterizations of Heterojunction Photocatalysts with Perovskite and Tin Sulfide Nanocrystals for Photocatalytic CO2 Reduction

Atul H. Bhosale, Sudhakar Narra, Rohit R. Koli, I-Hua Tsai, and Eric Wei-Guang Diau\*



Cite This: ACS Appl. Energy Mater. 2025, 8, 14804-14812



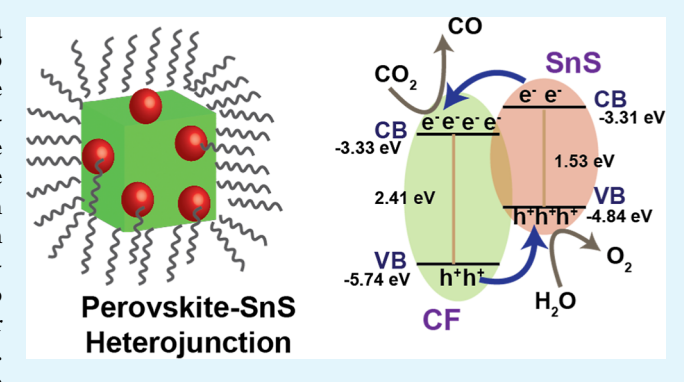
ACCESS I

Metrics & More

Article Recommendations

Supporting Information

ABSTRACT: Nanocrystal-nanocrystal heterojunctions play a prominent role in tuning the optical properties of materials to attain desired functionalities. In the realm of perovskite heterojunctions for photocatalysis, coupling between two nanocrystals is less explored, as perovskite nanocrystals were predominantly coupled with 2D sheets. Herein, we report the synthesis and photocatalytic activities of cesium formamidinium lead bromide (CF) perovskite nanocrystal heterojunctions with tin(II) sulfide (SnS) nanocrystals. Thorough structural, morphological, and charge transport dynamics studies were presented to confirm the formation of heterojunctions and to affirm their potential in imparting efficient charge separation at the interface. The prepared heterojunctions were shown to improve the



photocatalytic ability of aged CF nanocrystals by improving crystallinity and retarding phase transformations. The CF/SnS heterojunction sample prepared by mixing in the ratio of 5:1 has been shown to produce an impressive photocatalytic activity in the  $CO_2$  reduction to yield a CO yield of 153.1  $\mu$ mol g<sup>-1</sup> h<sup>-1</sup> with high product selectivity. Morphological, crystalline, and optical characterizations have been performed to understand the photocatalytic mechanism of CO<sub>2</sub> reduction using the CF/SnS heterojunction photocatalyst.

KEYWORDS: photocatalytic CO<sub>2</sub> reduction, perovskite nanocrystals, tin sulfide, TCSPC, TAS, type-II heterojunction

## 1. INTRODUCTION

Global warming due to increased carbon dioxide (CO<sub>2</sub>) emissions and energy shortages due to depletion of fossil fuels are the primary concerns for our environment. Mimicking the photosynthesis of plants by utilizing sunlight, artificial photosynthesis, such as reducing CO2 to produce clean fuels is an elegant way to circumvent global warming and reduce our dependence on conventional fossil fuel sources. 1-6 Following the pioneering works of Halmann and Honda, 7,8 large research activity is extended to reduce CO2 to produce valuable products, such as CO, CH<sub>4</sub>, CH<sub>3</sub>OH, HCHO, and so on using inorganic, organometallic, 2D materials and nanocrystals as photocatalysts. <sup>6,9–11</sup> However, the yields of the photocatalytic reactions have yet to reach the optimum levels.

Organo-inorganic halide perovskites are being investigated for their photocatalytic activity in recent years due to the simple preparation procedures, tunable optical band gaps, and impressive optoelectronic properties. 12-15 In the realm of perovskite photocatalysis, perovskite heterojunctions (PHJs) due to their superior stability, enhanced charge separation, broader light harvesting ability, and suppressed charge recombination. 14,16-20 For example, cesium lead bromide (CS) perovskite nanocrystal heterojunctions of Type-II, Zscheme, and S-scheme with various 3D and 2D materials such

as titanium dioxide (TiO<sub>2</sub>),<sup>21-24</sup> bismuth oxy halides (BiOX),<sup>25,26</sup> MXene sheets,<sup>18</sup> bismuth vanadate oxide (BiVO<sub>4</sub>),<sup>27</sup> reduced-graphene oxide (r-GO),<sup>28,29</sup> bismuth ferrite oxide (BiFeO<sub>3</sub>),<sup>30</sup> graphitic-carbon nitride (g-C<sub>3</sub>N<sub>4</sub>),<sup>31,32</sup> molybdenum nitride (MoN),<sup>19</sup> and so on, have shown enhanced photocatalytic performances than their pristine counterparts. However, studies employing nanocrystal-nanocrystal coupling to create heterostructures with perovskite nanocrystals for photocatalysis are limited.

Nanocrystal-nanocrystal heterostructures are advantageous over traditional heterostructures due to their ease of preparation using low-temperature solution processes and relaxed lattice matching constraints and offer seamless tunability of band structures and interfaces. Further, they have the ability to utilize the quantum effects to tune band gaps, improve absorption, enhance the surface-to-volume ratio, tune atomic orientations, and relax lattice strains that play a

Received: August 13, 2025 Revised: September 9, 2025 Accepted: September 10, 2025 Published: September 15, 2025





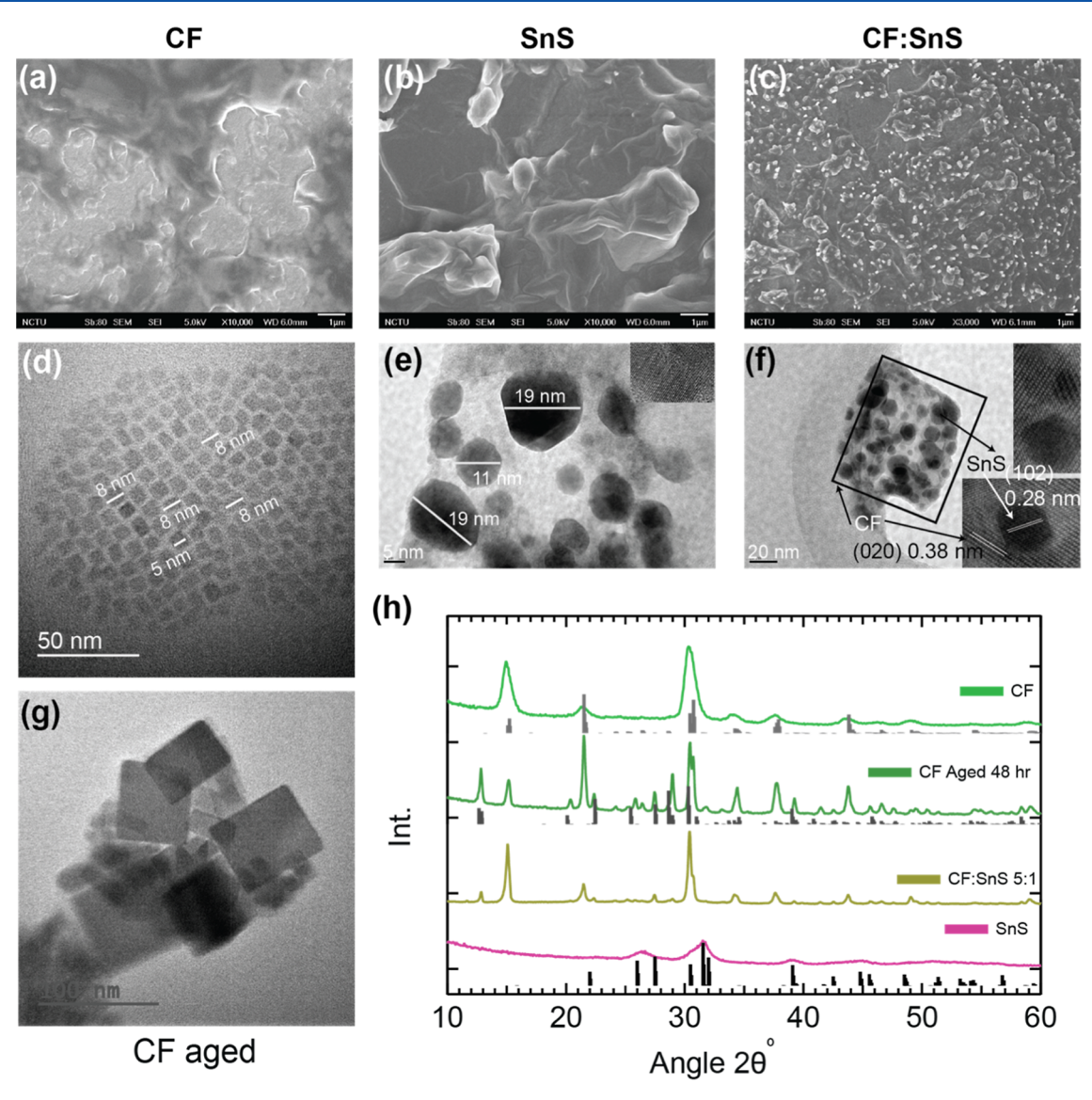


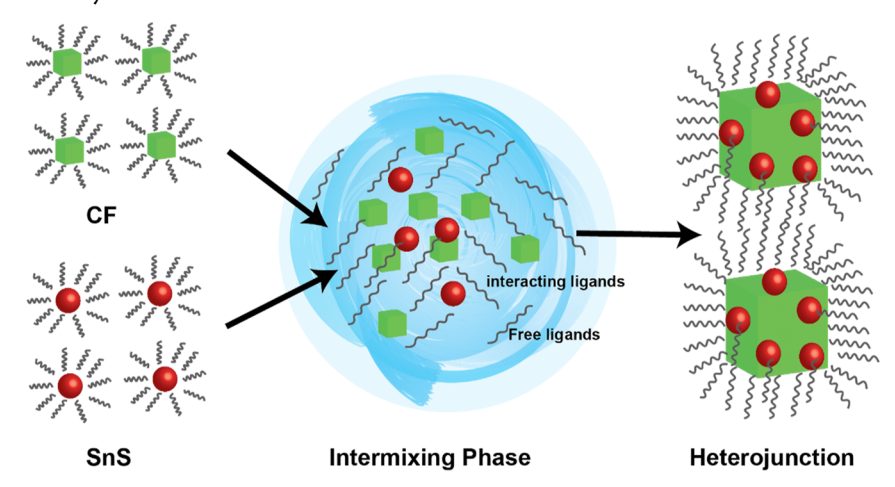
Figure 1. (a–c) Scanning electron microscopic images, (d–g) transmission electron microscopic images and (h) X-ray diffraction patterns of pristine CF, pristine SnS, and CF/SnS (5:1) heterojunction samples. Insets of (e,f) show lattice fringes of SnS and CF. The underneath sticks in the XRD patterns are CIF files of orthorhombic CsPbBr<sub>3</sub> (COD 4510745), hexagonal Cs<sub>4</sub>PbBr<sub>6</sub> (COD 4002857), and orthorhombic SnS (COD 1011253).

prominent role in the reactivity and carrier recombination dynamics of the materials. 17,33-35 Cadmium chalcogenide heterostructures such as CdS-PbS and CdTe-PbSe have been utilized in the fabrication of quantum dot solar cells, LEDs, and solar-to-fuel conversion processes. 33,35-37 However, challenges such as colloidal stability, disordered interfaces, and low mobilities exist to tap the full potential of these heterojunctions for photocatalytic and optoelectronic applications. In the case of perovskite nanocrystals, their colloidal stability has been shown to be improved by mixing with other low-dimensional materials, making them suitable for fabricating nanocrystalnanocrystal heterojunctions. Aging of perovskite nanocrystals leads to an increase in particle size due to Ostwald ripening and a significant decrease in photocatalytic activity, whereas wrapping them with appropriate low-dimensional materials improves their colloidal stability and photocatalytic performances. In our past work, we have shown the effects of aging on the photocatalytic activity of CF perovskite nanocrystals and

how a heterojunction with 2D BiVO<sub>4</sub> could rejuvenate the lost photocatalytic activity.<sup>38</sup>

Herein, we demonstrated the fabrication and photocatalytic activities of nanocrystal-nanocrystal heterojunctions utilizing tin sulfide (SnS) (a p-type indirect band gap semiconductor) and cesium formamidinium lead bromide (CF) perovskite nanocrystals (n-type) with band gaps in the near-infrared and visible regions, respectively. SnS nanocrystal heterojunctions used in photocatalysis and solar cells have demonstrated good performance.<sup>39-42</sup> The CS/SnS couple was shown to form a Type-II heterojunction, which offers good charge separation at the interface and is suitable for both photocatalysis and solar cells. Our results showed that CF/SnS heterojunction prepared by mixing precursors in the ratio of 5:1 resulted in a good quality sample that led to the realization of efficient charge separation at the interface to produce CO yields of 153.1 µmol  $g^{-1} h^{-1}$  in photocatalytic reduction of CO<sub>2</sub>, in comparison to 76.1  $\mu$ mol g<sup>-1</sup> h<sup>-1</sup> for pristine CF sample. The CO yields

Scheme 1. Schematic Showing Formation of the Heterojunction between CF and SnS Nanoparticles via Dynamic Intermixing and Regrowth of CF Nanocrystals



presented in this work are the highest reported for CF perovskite nanocrystal heterojunctions.

### 2. RESULTS AND DISCUSSION

## 2.1. Structural and Morphological Characterizations.

The CF perovskite nanocrystal (PeNC) and SnS nanocrystal samples were synthesized following the hot addition methods described in the Supporting Information. The morphologies and crystal structures of synthesized pristine nanocrystal samples shown in Figure 1, match very well with the published results. 26,43 The CF sample (Figures 1d, S1a-c) shows uniformly distributed cubic-shaped crystals with sizes of 5-8 nm with crystallographic planes (Figure 1h) associated with both orthorhombic and cubic phases. Similarly, the SnS sample (Figure 1e) shows 10-20 nm round disc-shaped nanoparticles with crystallographic planes (Figure 1h) associated with the orthorhombic phase.<sup>44</sup> The CF/SnS (5:1) sample showed a larger CF crystal (Figure 1f) underneath the small SnS nanoparticles atop. The increase in the size of CF PeNCs in heterojunction samples is the aging effect due to stirring in the process of synthesizing heterojunction samples, as the pristine CF PeNCs also demonstrated an increment in sizes (Figure 1g) and a change of phase to Cs<sub>4</sub>PbBr<sub>6</sub> (Figure 1h) in the absence of SnS when stirred for 48 h. HR-TEM images shown in the insets of Figure 1e,f show lattice fringes of SnS and CF crystallographic planes corresponding to a d-spacing of 0.38 nm for CF and 0.28 nm for SnS samples, corresponding to (020) and (120) orientations of the respective orthorhombic phases. The (020) orientation of CF is terminated via bromine atoms, while the (120) orientation of SnS is terminated via sulfur atoms, as shown in Figure S2, where strong interactions between Sn<sup>2+</sup> in SnS and Br- in CF might be responsible for the formation of heterojunctions via formation of chemical bonds similar to CsPbBr3 heterojunctions with respect to BiOBr, Bi<sub>2</sub>WO<sub>6</sub>, and BiOI. 25,26,45

**2.2.** Heterojunction Formation. The formation of a heterojunction between CF and SnS can be visualized from the schematic shown in Scheme 1. When CF and SnS nanocrystal samples were vigorously stirred during the intermixing phase, surface ligand detachments and formation of dangling bonds on the surfaces occurred for both nanocrystals. As perovskite nanocrystals are softer ionic lattices and are known for their rapid growth of crystalline size via Ostwald ripening mechanism, <sup>46</sup> CF grows in size and both CF and SnS

approach each other due to electrostatic interactions and the heterojunction formation happens via stabilization of the orthorhombic phase and formation of chemical bonds between  $\mathrm{Br}^-$  ions of CF and  $\mathrm{Sn}^{2+}$  ions as described above.

The XRD patterns of pristine CF, SnS, aged CF, and CF/ SnS (5:1) samples were simulated by using TOPAS software (Figure S4). The fitting procedures of the simulations were described in the experimental section of the Supporting Information. XRD simulations suggest that both pristine CF and SnS are predominantly orthorhombic (Figure S4), whereas aging of pristine CF leads to conversion of the orthorhombic and cubic phases to the hexagonal phase. However, the aging of CF in the presence of SnS suppresses the formation of hexagonal phase Cs<sub>4</sub>PbBr<sub>6</sub> due to the formation of a heterojunction between the two nanocrystals. The suppression of the hexagonal phase and stabilization of the orthorhombic phase align well with the minimal lattice match condition for the formation of a heterojunction between the counterparts in the CF/SnS (5:1) sample. The driving force for the formation of this heterojunction is via defect-mediated restructuring of CF perovskites into bigger crystals as described above. Photoluminescence quantum yield (PLQY) data of aged CF samples support the defect mediation as discussed later.

The formation of a heterojunction was determined by measuring the X-ray photoelectron spectra of pristine CF, SnS, and CF/SnS (5:1) samples, as shown in Figure S5. The highresolution XPS spectra were obtained for CF and CF/SnS (5:1) samples corresponding to Pb 4f and Sn 3d elements. The CF sample shows two bands at 138.1 and 143.0 corresponding to Pb<sup>2+</sup>  $^{2+}$   $^{2+}$  4f<sub>7/2</sub> and 4f<sub>5/2</sub>, respectively. For the heterojunction sample, these bands shift to higher binding energies by about 0.3 eV. Similarly, the SnS sample shows two bands at 486.5 and 495.0 corresponding to Sn 3d<sub>5/2</sub> and 3d<sub>3/2</sub>, respectively. 47,48 For the heterojunction sample, these bands shift to lower binding energies by about 0.5 eV. The shifts in binding energies of  $P \dot{b}^{2+}$  and  $S n^{2\dot{+}}$  suggest that electron transfer occurs from CF to SnS due to the formation of a heterojunction between CF and SnS. Further, valence band potentials were estimated for the CF, SnS, and CF/SnS samples from valence XPS measurements to probe the effects of heterojunctions on the valence band level of the heterojunction sample. The valence band XPS plots are shown in Figure S6, and the estimated potentials are 1.3, 0.4, and 1 eV, respectively, for the CF, SnS, and CF/SnS (5:1) samples. The shift of the valence

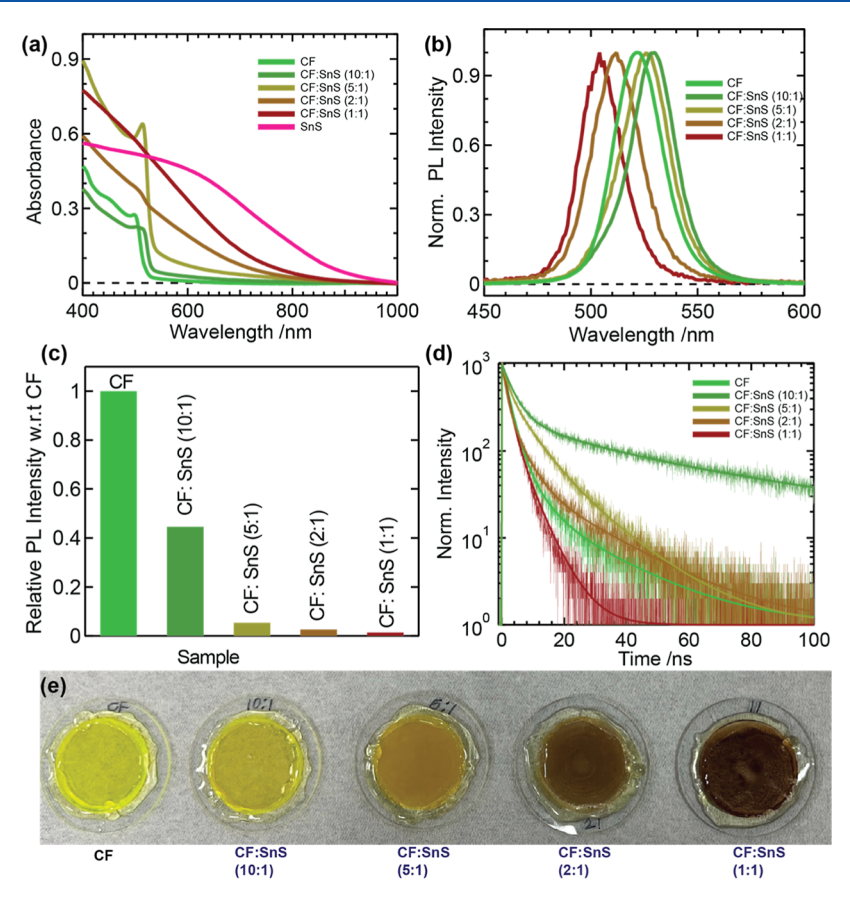


Figure 2. (a) UV-vis absorption spectra, (b) PL spectra, (c) PL relative intensities, (d) TCSPC decay profiles, and (e) photo images of pristine CF and heterojunction samples of CF with SnS.

potential of the CF/SnS (5:1) sample aligns well with the supposition of the formation of a heterojunction.

2.3. Optical Properties of the Heterojunction. The optical properties of the heterojunction samples, together with their pristine samples, were investigated using steady-state absorption, photoluminescence (PL), and time-correlated single photon counting techniques (TCSPC) as shown in Figure 2. The absorption spectra of the synthesized pristine CF and heterojunction samples show band edges at 524, 534, and 538 nm, respectively, for CF, 10:1, and 5:1 samples, in line with the observed color changes of the films shown in Figure 2e. However, higher ratio samples, namely, 2:1 and 1:1, together with SnS, do not show a definite band edge characteristic of excitons. The band edge of pristine CF matches the reported values for the 7-10 nm crystals. <sup>26,49</sup> The red shift of the band edge for heterojunction samples could be due to the cumulative effect of changes in particle sizes and interactions of CF nanocrystals with SnS nanocrystals in forming the heterojunction. The HR-TEM images of the heterojunction and aged CF samples shown in Figure 1 show an increase in crystal size compared to that of the pristine CF sample. As the heterojunction involves stirring for 48 h, the effects of aging on the changes in particle sizes and band gaps cannot be ruled out. The PL spectrum of aged CF is shown in Figure S7. The PL spectrum of aged CF shows a red shift compared to fresh CF due to particle size and composition changes as discussed above. However, the observed shifts are larger in the higher SnS-concentration samples; a simple particle size cannot induce these shifts. Due to a lack of a proper band edge, quantification of the absorption onset has

become challenging for these samples. But, the shifts in absorption spectrum are indicative of interactions between CF/SnS nanostructures, which may lead to the formation of a heterojunction with distinctive optical properties compared to their pristine counterparts. Similar to absorption, the PL spectra of heterojunction samples, namely, 10:1 and 5:1 show red shifts in the PL maxima with the observed PL maxima at 522, 530, and 526 nm, respectively, for the pristine CF, 10:1, and 5:1 samples. However, the heterojunction samples with higher blend ratios of 2:1 and 1:1 show blue shifts in the PL maxima with peak positions at 512 and 504 nm, respectively. The PL spectra started to recede from 530 nm to shorter wavelengths from a 5:1 ratio sample. The blue shifts in these higher mixing ratios might be due to significant changes in the band structure of CF at these samples. The shifts of PL maximum cannot be assigned to size changes alone, as the aging sample with larger particle sizes showed red shift in PL maximum (Figure S7). The blue shifts in PL maxima are indicative of heterojunction formation between the CF and SnS samples. Apart from the peak shifts, the heterojunction samples show quenching in the PL intensities with an increased ratio of SnS, as shown in Figure 2c. The quenching in the PL intensities can be attributed to charge separation at the interface and quenching caused by defects at the interface. PLQY experiments were conducted to further understand the decrease in the observed PL intensities. The PLQY values are tabulated in Table S2. The PLQY values decrease with an increase in the SnS concentration. Aging of pristine CF also decreases the PLQY. Pristine CF shows a PLQY 0.8, whereas aging reduces the PLQY by a factor of 10-0.08. In contrast,

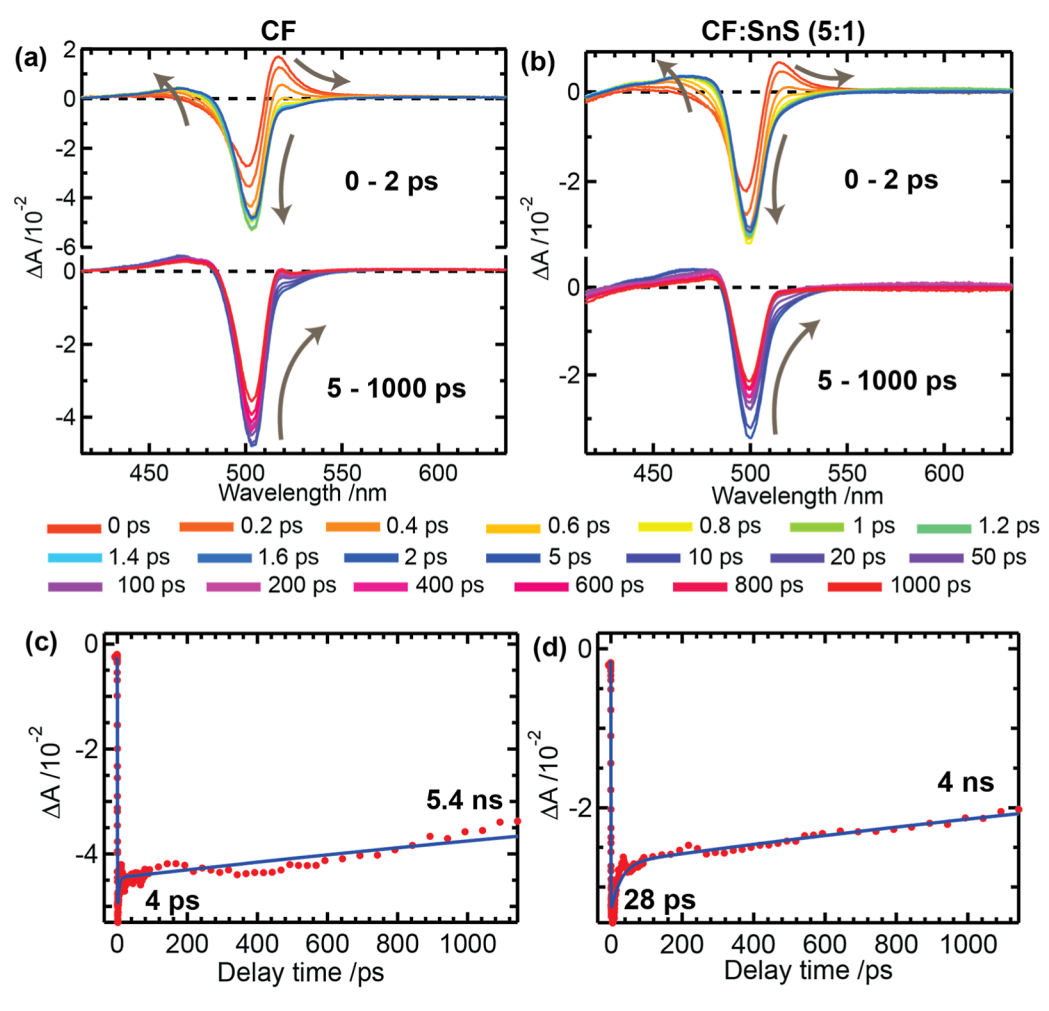


Figure 3. Femtosecond transient absorption spectra and kinetics of (a,c) CF nanocrystals and (b,d) CF/SnS (5:1) nanocrystal heterojunction samples dispersed in toluene. Transient kinetics are taken at the bleach minima. The excitation wavelength was set to 325 nm.

aging in the presence of SnS decreases PLQY but not to the extent of the decrease without SnS, with values of 0.66, 0.56, 0.48, and 0.38, respectively, for 10:1, 5:1, 2:1, and 1:1 ratio samples. Thus, the drop in PL intensities and PLQY indicates activation of nonradiative pathways. To gain more insight into the quenching mechanisms, both TCSPC and femtosecond transient absorption spectral (fs-TAS) experiments were performed.

**2.4. TCSPC Decay Profiles.** The TCSPC decay profiles of pristine CF, aged CF, and CF/SnS heterojunction samples are shown in Figure 2d. All of the observed decay profiles were fitted with a triple exponential function to maintain a similar fitting model for all the samples, though the amplitudes of third components were low for some compositions. The faster and closely decaying components  $\tau_1$  and  $\tau_2$  can be assigned to radiative recombination due to different crystallographic phases or different-sized crystals. In contrast, the slower decaying component  $\tau_3$  can be assigned to trap-state-mediated recombination. Pristine CF samples with narrower (Figure 2) and broader (Figure S7) spectra show that TCSPC decay profiles predominantly decay rapidly within 10 ns with a very minor  $\tau_3$  component, in line with the observed higher PLQY of 0.81. However, the aged CF sample displays a much longer average lifetime of 57 ns despite a poorer PLQY of 0.08. The longer lifetime of the aged CF sample is due to the increased amplitude of the slower decaying component  $\tau_3$ , which alone

decays with a time constant of 90 ns. Aging of the CF sample increased the particle size and also induced new hexagonal phase formation, which led to a drop in PLQY and opened up the shallow trapped-state-mediated recombination channel. Similarly, the 10:1 sample also displayed similar behavior to the aged CF sample as this sample also shows predominant hexagonal phases with poorer crystallinity (Figure S3). However, 5:1, 2:1, and 1:1 samples showed suppression of the amplitude of the slower decaying component  $\tau_3$  and a decrease of lifetimes compared with the aged CF sample. The decrease in the lifetimes of faster decaying components  $\tau_1$  and  $\tau_2$ , along with a gradual decrease in PLQY for 5:1, 2:1, and 1:1, is indicative of charge separation in addition to defectmediated recombination (Table S1). However, the 5:1 sample is shown to perform better than the higher concentration analogs 2:1 and 1:1 in the photocatalytic experiments. The crystallinity of 2:1 and 1:1 is inferior compared to 5:1, and an increase in surface coverage of CF with SnS might lead to a decrease in absorption in the native CF, which have led to the poor performance of the higher concentration samples.

**2.5. Femtosecond TAS Study.** Femtosecond TAS spectra of CF, CF/SnS (5:1) heterojunction, and SnS samples are recorded using an excitation pulse at 325 nm. The femtosecond TAS profiles and the kinetics of pristine CF and CF/SnS heterojunction samples are shown in Figure 3, whereas those of the pristine SnS sample are shown in Figure S9. The

TAS profiles of pristine CF and CF/SnS heterojunction samples show photobleach (PB) bands at 504 and 500 nm, respectively, due to the depletion of the lowest exciton transition and photoinduced absorption (PIA) bands as wings on both sides of the main PB band. The PB band shows evolution, and the PIA band on the low-energy side shows decay within the first two ps associated with the thermalization of carriers. After thermalization subsides, recovery of PB and PIA bands can be seen for the recorded spectra for up to 1 ns. The transient kinetics of the PB bands show carrier relaxation dynamics and underlying mechanistic differences between pristine CF and the CF/SnS heterojunction samples. The transient decay profiles of the PB bands of these two samples show two decaying components: a faster picosecond decaying component and a slower nanosecond decaying component. The faster picosecond component with a time constant of 4 ps in the pristine CF sample can be assigned to carrier trapping to shallow trap states, whereas the nanosecond decaying component can be assigned to radiative recombination, as shown in the TCSPC decays. The faster decaying component slowed to 28 ps in the heterojunction sample due to the interfacial charge separation process and modulation in the density of trap states at the interfaces due to heterojunction formation. Further, the nanosecond component in the heterojunction sample can also be assigned to radiative recombination similar to the pristine CF sample. Additionally, charge separation at the interface is probed by monitoring the thermalization rates from their respective PIA band maxima at 517 and 515 nm for CF and CF/SnS heterojunction samples. The heterojunction sample showed faster relaxation of hot carriers due to carrier injection to SnS compared to the CF sample with time constants of 250 and 350 fs, respectively, for CF/SnS and CF samples, as shown in Figure S8. The faster charge injection and slower recombination reveal both interfacial dynamics and retarded recombination due to the creation of defects in the heterostructure sample. The retarded recombination via defects was shown to be beneficial for CO<sub>2</sub> reduction in our earlier work.

The TAS profiles of SnS show a broad PIA band in the range of 450-650 nm (Figure S9), which shows a rapid evolution and decay within 100 ps. The PIA bands are assigned to absorption from trap states of SnS nanocrystals. 50,51 The transient kinetics of SnS also show double exponential decay, similar to the other two samples discussed above. The faster component decays within 1.3 ps, while the slower component decays within 53 ps. The faster component can be assigned to thermalization of carriers, whereas the slower component can be assigned to trap-state-mediated recombination. The observed TAS profiles and kinetics of SnS agree with the published reports elsewhere. 50,51 It is important to note that the heterojunction sample produces signals only from CF nanocrystals, despite SnS nanocrystals also being able to be excited at this pump wavelength, indicating weaker absorption due to a smaller concentration of SnS compared with pristine CF in the measured composition. Thus, the measured transient kinetics of the CF/SnS heterojunction sample can be safely ignored for any interference from SnS excitation. Thus, the TAS experiments clearly indicate heterojunction formation and charge separation at the interfaces that are suitable for photocatalytic experiments.

**2.6. Photocatalytic Activity.** The CO<sub>2</sub> photocatalytic reduction experiments were conducted following the procedures outlined in our earlier works. A brief experimental

procedure is provided in the Supporting Information. In these experiments,  $CO_2$  gas was passed through water before filling the reactor, and the reactor was illuminated under 1 sun (1000 W m<sup>-2</sup>). The photoproducts obtained from the reaction were analyzed every few hours using gas chromatography (GC). CF and heterojunction samples show predominantly CO yields, as shown in Figure 4. The yields of CO for pristine CF under

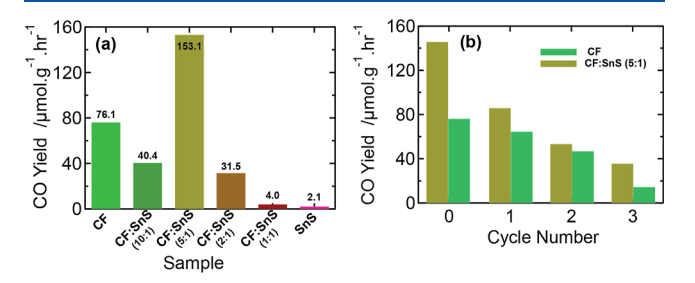


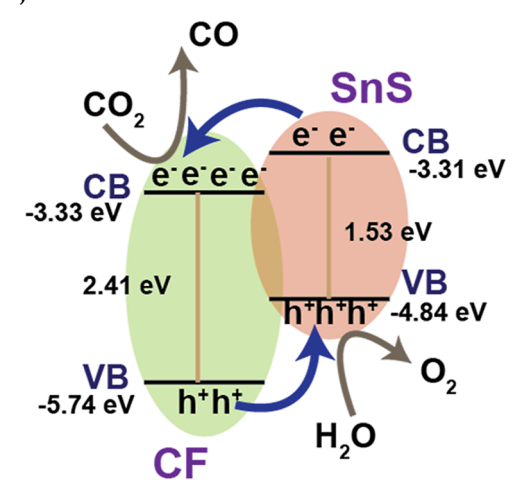
**Figure 4.** (a) The photocatalytic yields of CO formation for CF, SnS, and CF/SnS heterojunction samples in the ratios of 10:1, 5:1, 2:1, and 1:1. (b) Recycling effects on the photocatalytic yields of CO formation for CF and CF/SnS (5:1) heterojunction samples.

humid environments are consistent or slightly better than our earlier works. The observed yields of CO for pristine CF, aged CF, 10:1, 5:1, 2:1, 1:1, and SnS are  $76.1 \pm 14$ ,  $21.5 \pm 2$ ,  $40.4 \pm 14$ 6, 153.1  $\pm$  7, 31.5  $\pm$  1, 4.0  $\pm$  1.4, and 2.1  $\pm$  0.4  $\mu$ mol g<sup>-1</sup> h<sup>-1</sup>, respectively. The yields of CO decrease for CF heterojunctions compared to pristine CF, except for the 5:1 ratio sample. The decrease in the yields of CO for 10:1 can be due to the formation of hexagonal phases, as shown in the XRD (Figure S3), whereas 2:1 and 1:1 samples lose their crystallinity and light-harvesting ability as shown in their XRD (Figure S3) and absorption spectra (Figure 2). However, the 5:1 sample shows enhanced crystallinity and suppressed hexagonal phases compared to other ratios, leading to a better interface formation with SnS. The increase in product yield for the 5:1 sample can also be assigned to an increase in the availability of more protons due to the formation of the hexagonal phase by the expulsion of FA cations, analogous to the case of the cubic phase we proposed in our earlier work.<sup>43</sup> Further, photocurrent experiments of CF, SnS, and CF/SnS (5:1) samples showed that the heterojunction sample showed twice the magnitude of photocurrent compared to pristine CF due to efficient charge separation at the interface, which led to an enhancement in the photocatalytic activity (Figure S10). The obtained yield of CO for the 5:1 sample is the highest reported so far for CF or CS heterojunction samples measured under gas-solid interface reaction conditions. Furthermore, the photocatalyst recycling tests also show that the CF/SnS heterojunction is superior to pristine CF for the product yields (Figure 4b) and the product yields show fair linearity for a period of 80 h as shown in Figure S11. The stability of the photocatalysts was monitored by measuring the TEM and XRD of the recycled photocatalysts as shown in Figure S12. The morphologies of the pristine CF sample showed the growth of rod-like structures, while the CF/SnS 5:1 sample retained its morphology. The XRD pattern of pristine CF shows minor peaks of hexagonal phases after photocatalysis experiments, whereas the CF/SnS sample showed further suppression of hexagonal phases due to stabilization of the orthorhombic phases at the heterojunction during irradiation.

**2.7. Mechanism of Enhanced Photocatalytic Activity.** The mechanism behind the enhanced photocatalytic activity of

the heterojunction sample can be understood based on the type of heterojunction formed and charge separation at the interfaces. The valence band (VB) and conduction band (CB) levels with respect to vacuum were estimated by combining the estimated valence band potentials ( $E_{\rm abs} = -E^{\Phi} - 4.44$ ;  $^{52}E_{\rm abs} =$  vacuum energy and  $E^{\Phi} =$  normal electrode potential) (Figure S6) and band gaps estimated from the Tauc plots of CF and SnS samples (Figure S13). The estimated VB levels for CF and SnS are -5.74 eV and -4.84 eV, respectively, and the estimated band gaps (Figure S13) are 2.41 and 1.53 eV, respectively. Further, the calculated CB levels for CF and SnS are -3.33 eV and -3.31 eV, respectively. The alignments of VB and CB facilitate the formation of a Type-II heterojunction, as shown in Scheme 2. Further, theoretical calculations also

Scheme 2. Mechanism of  ${\rm CO_2}$  Reduction in the CF/SnS Heterojunction Facilitated by the Formation of a Type-II Heterojunction



# **Type-II Heterojunction**

suggest that cesium lead bromide nanocrystals form a Type-II heterojunction with SnS nanoparticles. Sa As the band gap of CF is close to that of CS, a similar type of heterojunction can be expected between CF and SnS nanoparticles. The reported valence band offsets of similar type CF and SnS samples at -6.1 and -5.1 eV, respectively, also suggest that hole transfers from CF to SnS upon photoexcitation are very much probable, leading to charge separation at the interface. At the same time, the electron remains on the CF surface to be utilized in the CO<sub>2</sub> reduction for the efficient production of CO.

## 3. CONCLUSIONS

In summary, a nanocrystal—nanocrystal heterojunction photocatalyst between CF and SnS was synthesized using a simple stirring approach at room temperature. The ratios between CF and SnS were optimized to improve the crystal quality and optical properties to attain higher photocatalytic activities than pristine CF. The formation of heterojunction samples was confirmed from HR-TEM, PL, XPS, TCPSC, and fs-TAS experiments. The hexagonal phases of aged CF samples were also suppressed in the 5:1 ratio CF/SnS heterojunction sample, which demonstrated good crystallinity compared to other heterojunction samples. Both TCSPC and fs-TAS experiments confirmed the charge separation at the interfaces for the heterojunction samples. The CF/SnS, 5:1 ratio sample

was shown to achieve an impressive CO yield of 153.1  $\mu mol\ g^{-1}\ h^{-1}$  compared to the pristine CF giving 76.1  $\mu mol\ g^{-1}\ h^{-1}$  with good selectivity. The heterojunction sample was shown to perform better than the CF sample under recycling tests. The enhanced performance of CF/SnS heterojunctions can be attributed to the formation of a Type-II heterojunction, which led to efficient charge separation and utilization of conduction band electrons for the CO $_2$  reduction reactions. This study, therefore, presents an alternative approach to stabilize the aged perovskite nanocrystals to produce much more efficient yields of CO than perovskite-2D sheet heterojunctions. The demonstrated nanocrystal—nanocrystal heterojunction offers an alternative approach to design efficient perovskite nanocrystal-based photocatalysts.

### ASSOCIATED CONTENT

## Supporting Information

The Supporting Information is available free of charge at https://pubs.acs.org/doi/10.1021/acsaem.5c02530.

Synthesis procedures, experimental methods, TEM images, XRD, XPS, PL, TCSPC decays, photocurrent, Tauc plots, and TAS profiles of nanocrystal samples (PDF)

#### AUTHOR INFORMATION

## **Corresponding Author**

Eric Wei-Guang Diau — Department of Applied Chemistry, Institute of Molecular Science, National Yang Ming Chiao Tung University, Hsinchu 300093, Taiwan; Center for Emergent Functional Matter Science, National Yang Ming Chiao Tung University, Hsinchu 300093, Taiwan; orcid.org/0000-0001-6113-5679; Email: diau@nycu.edu.tw

#### Authors

Atul H. Bhosale – Department of Applied Chemistry, Institute of Molecular Science, National Yang Ming Chiao Tung University, Hsinchu 300093, Taiwan

Sudhakar Narra — Department of Applied Chemistry, Institute of Molecular Science, National Yang Ming Chiao Tung University, Hsinchu 300093, Taiwan; Center for Emergent Functional Matter Science, National Yang Ming Chiao Tung University, Hsinchu 300093, Taiwan; orcid.org/0000-0003-4893-9204

Rohit R. Koli – Department of Applied Chemistry, Institute of Molecular Science, National Yang Ming Chiao Tung University, Hsinchu 300093, Taiwan

I-Hua Tsai – Department of Applied Chemistry, Institute of Molecular Science, National Yang Ming Chiao Tung University, Hsinchu 300093, Taiwan

Complete contact information is available at: https://pubs.acs.org/10.1021/acsaem.5c02530

#### Notes

The authors declare no competing financial interest.

## ACKNOWLEDGMENTS

We gratefully acknowledge the support of the National Science and Technology Council (NSTC), Taiwan, (grants: NSTC 113-2639- M-A49-001-ASP and NSTC 114-2639-M-A49-001-ASP) and the Center for Emergent Functional Matter Science of National Yang Ming Chiao Tung University (NYCU) from

the Featured Areas Research Center Program within the framework of the Higher Education Sprout Project by the Ministry of Education (MOE) in Taiwan.

### REFERENCES

- (1) Peter, S. C. Reduction of CO2 to Chemicals and Fuels: A Solution to Global Warming and Energy Crisis. ACS Energy Lett. **2018**, 3 (7), 1557–1561.
- (2) Barros, V.; Field, C. B.; Dahe, Q.; Stocker, T. F. Managing the Risks of Extreme Events and Disasters to Advance Climate Change Adaptation; Cambridge University Press, 2012.
- (3) Peterman, K. E.; O'Keefe, K. T. V.; Melton, H. P.; Lestrange, P. J.; Sobhy, M.; Jones, R.; Kovil, N.; Civitella, M.; Snier, Z. J.; White, J. L.; Pothoof, J.; O'Keefe, K. T. V.; Henderson, A. N.; Foy, G. P.; Foy, R. L. H.; Cordes, M. R. Global Consensus on Climate Change: Paris Agreement and the Path Beyond. ACS Symposium Series, 1313; American Chemical Society, 2019.
- (4) Sanderson, K. COP28 Climate Summit Signals the End of Fossil Fuels—but Is It Enough? Nature 2023, 624, 484-485.
- (5) Chu, S.; Cui, Y.; Liu, N. The Path towards Sustainable Energy. Nat. Mater. 2017, 16 (1), 16-22.
- (6) Ramirez-Corredores, M. M. Sustainable Production of CO<sub>2</sub>-Derived Materials. npj Mater. Sustain. 2024, 2 (1), 35.
- (7) Halmann, M. Photoelectrochemical Reduction of Aqueous Carbon Dioxide on P-Type Gallium Phosphide in Liquid Junction Solar Cells. Nature 1978, 275 (5676), 115-116.
- (8) Inoue, T.; Fujishima, A.; Konishi, S.; Honda, K. Photoelectrocatalytic Reduction of Carbon Dioxide in Aqueous Suspensions of Semiconductor Powders. Nature 1979, 277 (5698), 637-638.
- (9) Wu, J.; Huang, Y.; Ye, W.; Li, Y. CO<sub>2</sub> Reduction: From the Electrochemical to Photochemical Approach. Adv. Sci. 2017, 4 (11), 1700194.
- (10) Fang, S.; Rahaman, M.; Bharti, J.; Reisner, E.; Robert, M.; Ozin, G. A.; Hu, Y. H. Photocatalytic CO2 Reduction. Nat. Rev. Methods Prim. 2023, 3 (1), 61.
- (11) Kovačič, Ž.; Likozar, B.; Huš, M. Photocatalytic CO 2 Reduction: A Review of Ab Initio Mechanism, Kinetics, and Multiscale Modeling Simulations. ACS Catal. 2020, 10 (24), 14984-15007.
- (12) Shyamal, S.; Pradhan, N. Halide Perovskite Nanocrystal Photocatalysts for CO2 Reduction: Successes and Challenges. J. Phys. Chem. Lett. 2020, 11 (16), 6921-6934.
- (13) Raza, M. A.; Li, F.; Que, M.; Zhu, L.; Chen, X. Photocatalytic Reduction of CO 2 by Halide Perovskites: Recent Advances and Future Perspectives. Mater. Adv. 2021, 2 (22), 7187-7209.
- (14) Purohit, S.; Yadav, K. L.; Satapathi, S. Metal Halide Perovskite Heterojunction for Photocatalytic Hydrogen Generation: Progress and Future Opportunities. Adv. Mater. Interfaces 2022, 9, 2200058.
- (15) Wang, X.; He, J.; Chen, X.; Ma, B.; Zhu, M. Metal Halide Perovskites for Photocatalytic CO2 Reduction: An Overview and Prospects. Coord. Chem. Rev. 2023, 482, 215076.
- (16) Akinoglu, E. M.; Hoogeveen, D. A.; Cao, C.; Simonov, A. N.; Jasieniak, J. J. Prospects of Z-Scheme Photocatalytic Systems Based on Metal Halide Perovskites. ACS Nano 2021, 15 (5), 7860-7878.
- (17) Kipkorir, A.; DuBose, J.; Cho, J.; Kamat, P. V. CsPbBr3-CdS Heterostructure: Stabilizing Perovskite Nanocrystals for Photocatalysis. Chem. Sci. 2021, 12 (44), 14815-14825.
- (18) Pan, A.; Ma, X.; Huang, S.; Wu, Y.; Jia, M.; Shi, Y.; Liu, Y.; Wangyang, P.; He, L.; Liu, Y. CsPbBr 3 Perovskite Nanocrystal Grown on MXene Nanosheets for Enhanced Photoelectric Detection and Photocatalytic CO<sub>2</sub> Reduction. J. Phys. Chem. Lett. 2019, 10 (21), 6590-6597.
- (19) Hou, Y.; Song, X.; Zhang, Y.; Ren, T.; Wang, J.; Qin, J.; Yang, J.; Xie, Z.; Tian, Z.; Guan, Z.; Fu, X.; Jiao, S.; Li, Q.; Li, E. 0D/2D Schottky Heterojunction of CsPbBr3 Nanocrystals on MoN Nanosheets for Enhancing Charge Transfer and CO<sub>2</sub> Photoreduction. FlatChem. 2024, 47, 100720.

- (20) Zhang, Z.; Dong, Z.; Jiang, Y.; Chu, Y.; Xu, J. A Novel S-Scheme Heterojunction of CsPbBr<sub>3</sub> Nanocrystals/AgBr Nanorods for Artificial Photosynthesis. Chem. Eng. J. 2022, 435, 135014.
- (21) Xu, F.; Meng, K.; Cheng, B.; Wang, S.; Xu, J.; Yu, J. Unique S-Scheme Heterojunctions in Self-Assembled TiO2/CsPbBr3 Hybrids for CO2 Photoreduction. Nat. Commun. 2020, 11 (1), 4613.
- (22) Dong, Z.; Zhang, Z.; Jiang, Y.; Chu, Y.; Xu, J. Embedding CsPbBr3 Perovskite Quantum Dots into Mesoporous TiO2 Beads as an S-Scheme Heterojunction for CO2 Photoreduction. Chem. Eng. J. **2022**, *433*, 133762.
- (23) Sun, C.; Zhao, Y.; Ding, Y.; Zhang, F.; Deng, Z.; Lian, K.; Wang, Z.; Cui, J.; Bi, W. Efficient Homojunction/Heterojunction Photocatalyst via Integrating CsPbBr3 Quantum Dot Homojunction with TiO2 for Degradation of Organic Dyes. ACS Appl. Mater. Interfaces 2024, 16 (19), 24806-24815.
- (24) Wang, X.; Wang, H.; Zhang, H.; Yu, W.; Wang, X.; Zhao, Y.; Zong, X.; Li, C. Dynamic Interaction between Methylammonium Lead Iodide and TiO2 Nanocrystals Leads to Enhanced Photocatalytic H<sub>2</sub> Evolution from HI Splitting. ACS Energy Lett. 2018, 3 (5), 1159-1164.
- (25) Zhang, Z.; Li, L.; Jiang, Y.; Xu, J. Step-Scheme Photocatalyst of CsPbBr 3 Quantum Dots/BiOBr Nanosheets for Efficient CO<sub>2</sub> Photoreduction. Inorg. Chem. 2022, 61 (7), 3351-3360.
- (26) Bhosale, A. H.; Narra, S.; Bhosale, S. S.; Diau, E. W.-G. Interface-Enhanced Charge Recombination in the Heterojunction between Perovskite Nanocrystals and BiOI Nanosheets Serves as an S-Scheme Photocatalyst for CO2 Reduction. J. Phys. Chem. Lett. 2022, 13 (34), 7987-7993.
- (27) Tan, P.; Ren, R.; Yang, L.; Zhang, M.; Zhai, H.; Liu, H.; Chen, J.; Pan, J. Direct S-Scheme 0D/2D Photocatalyst of CsPbBr3 Quantum Dots/BiVO4 Nanosheets for Efficient CO<sub>2</sub> Photoreduction. J. Mol. Liq. 2024, 393, 123644.
- (28) Wu, Y.; Wang, P.; Zhu, X.; Zhang, Q.; Wang, Z.; Liu, Y.; Zou, G.; Dai, Y.; Whangbo, M.-H.; Huang, B. Composite of CH3NH3PbI3 with Reduced Graphene Oxide as a Highly Efficient and Stable Visible-Light Photocatalyst for Hydrogen Evolution in Aqueous HI Solution. Adv. Mater. 2018, 30 (7), 1704342.
- (29) Xu, Y.-F.; Yang, M.-Z.; Chen, B.-X.; Wang, X.-D.; Chen, H.-Y.; Kuang, D.-B.; Su, C.-Y. A CsPbBr 3 Perovskite Quantum Dot/ Graphene Oxide Composite for Photocatalytic CO 2 Reduction. J. Am. Chem. Soc. 2017, 139 (16), 5660-5663.
- (30) Pan, D.; Lu, Y.; Idris, A. M.; Chen, Z.; Xu, L.; Wang, J.; Jiang, G.; Chen, Z.; Li, Z. Enhancing Photocatalytic CO 2 Reduction via a Single-Domain Ferroelectric Z-Scheme Heterojunction of BiFeO 3/ CsPbBr 3 Inducing Dual Built-in Electric Fields. J. Mater. Chem. A **2024**, 12 (17), 10461–10471.
- (31) Zhang, S.; Wang, Y.; Mersal, G. A. M.; Alhadhrami, A.; Alshammari, D. A.; Wang, Y.; Algadi, H.; Song, H. Enhanced Photocatalytic CO2 Reduction via MXene Synergism: Constructing an Efficient Heterojunction Structure of g-C3N4/Nb2C/CsPbBr3. Adv. Compos. Hybrid Mater. 2024, 7 (6), 226.
- (32) Bian, H.; Li, D.; Wang, S.; Yan, J.; Liu, S.; Frank. 2D-C 3 N 4 Encapsulated Perovskite Nanocrystals for Efficient Photo-Assisted Thermocatalytic CO 2 Reduction. Chem. Sci. 2022, 13 (5), 1335-
- (33) Xiang, X.; Wang, L.; Zhang, J.; Cheng, B.; Yu, J.; Macyk, W. Cadmium Chalcogenide (CdS, CdSe, CdTe) Quantum Dots for Solar-to-Fuel Conversion. Adv. Photonics Res. 2022, 3 (11), 2200065. (34) Wu, K.; Lian, T. Quantum Confined Colloidal Nanorod
- Heterostructures for Solar-to-Fuel Conversion. Chem. Soc. Rev. 2016, 45 (14), 3781-3810.
- (35) Kim, S.; Fisher, B.; Eisler, H.-J.; Bawendi, M. Type-II Quantum Dots: CdTe/CdSe(Core/Shell) and CdSe/ZnTe(Core/Shell) Heterostructures. J. Am. Chem. Soc. 2003, 125 (38), 11466-11467.
- (36) Dagher, S.; Haik, Y.; Tit, N.; Ayesh, A. PbS/CdS Heterojunction Quantum Dot Solar Cells. J. Mater. Sci.: Mater. Electron. 2016, 27 (4), 3328-3340.
- (37) Liu, H.; Tian, Y.; Zhang, Y.; Gao, K.; Lu, K.; Wu, R.; Qin, D.; Wu, H.; Peng, Z.; Hou, L.; Huang, W. Solution Processed CdTe/

- CdSe Nanocrystal Solar Cells with More than 5.5% Efficiency by Using an Inverted Device Structure. *J. Mater. Chem. C* **2015**, 3 (17), 4227–4234.
- (38) Tsai, I.-H.; Kuo, Y.-R.; Hiramatsu, H.; Diau, E. W.-G. Enhanced Photocatalytic Performance for CO<sub>2</sub> Reduction via an S-Scheme Heterojunction between Perovskite Nanocrystals and BiVO 4. *J. Mater. Chem. A* **2025**, *13* (9), 6513–6523.
- (39) Omr, H. A. E.; Putikam, R.; Hussien, M. K.; Sabbah, A.; Lin, T.-Y.; Chen, K.-H.; Wu, H.-L.; Feng, S.-P.; Lin, M.-C.; Lee, H. Design of Sculptured SnS/g-C<sub>3</sub>N<sub>4</sub> Photocatalytic Nanostructure for Highly Efficient and Selective CO<sub>2</sub> Conversion to Methane. *Appl. Catal., B* **2023**, 324, 122231.
- (40) Jia, X.; Wang, J.; Lu, Y.; Sun, J.; Li, Y.; Wang, Y.; Zhang, J. Designing SnS/MoS 2 van Der Waals Heterojunction for Direct Z-Scheme Photocatalytic Overall Water-Splitting by DFT Investigation. *Phys. Chem. Chem. Phys.* **2022**, 24 (35), 21321–21330.
- (41) Jia, T.; Fu, F.; Li, J.; Deng, Z.; Long, F.; Yu, D.; Cui, Q.; Wang, W. Rational Construction of Direct Z-Scheme SnS/g-C<sub>3</sub>N<sub>4</sub> Hybrid Photocatalyst for Significant Enhancement of Visible-Light Photocatalytic Activity. *Appl. Surf. Sci.* **2020**, 499, 143941.
- (42) Wang, L.; Fu, L.; Yin, L. SnS Quantum Dot-CsPbBr3 Perovskite Bulk Heterojunction for Enhanced Photoelectrical Conversion Efficiency. Sol. RRL 2020, 4 (11), 2000417.
- (43) Bhosale, S. S.; Kharade, A. K.; Narra, S.; Chang, S.; Wei-Guang Diau, E. Self-Photocatalytic Splitting of Carbon Dioxide Using Co-Cationic Perovskite Nanocrystals in the Absence of Water. *ACS Energy Lett.* **2023**, 8 (1), 280–288.
- (44) Veerasubramani, G. K.; Park, M.-S.; Choi, J.-Y.; Kim, D.-W. Ultrasmall SnS Quantum Dots Anchored onto Nitrogen-Enriched Carbon Nanospheres as an Advanced Anode Material for Sodium-Ion Batteries. ACS Appl. Mater. Interfaces 2020, 12 (6), 7114–7124.
- (45) Wang, J.; Wang, J.; Li, N.; Du, X.; Ma, J.; He, C.; Li, Z. Direct Z-Scheme 0D/2D Heterojunction of CsPbBr 3 Quantum Dots/Bi<sub>2</sub>WO<sub>6</sub> Nanosheets for Efficient Photocatalytic CO 2 Reduction. ACS Appl. Mater. Interfaces 2020, 12 (28), 31477–31485.
- (46) DuBose, J. T.; Christy, A.; Chakkamalayath, J.; Kamat, P. V. Transformation of Perovskite Nanoplatelets to Large Nanostructures Driven by Solvent Polarity. *ACS Mater. Lett.* **2022**, *4* (1), 93–101.
- (47) Joy, S.; Atapattu, H. R.; Sorensen, S.; Pruett, H.; Olivelli, A. B.; Huckaba, A. J.; Miller, A.-F.; Graham, K. R. How Additives for Tin Halide Perovskites Influence the Sn 4+ Concentration. *J. Mater. Chem. A* **2022**, *10* (25), 13278–13285.
- (48) Wang, Y.; Xu, F.; Sun, L.; Li, Y.; Liao, L.; Guan, Y.; Lao, J.; Yang, Y.; Zhou, T.; Wang, Y.; Li, B.; Zhang, K.; Zou, Y. A Highly Active Z-Scheme SnS/Zn 2 SnO 4 Photocatalyst Fabricated for Methylene Blue Degradation. RSC Adv. 2022, 12 (49), 31985–31995.
- (49) Narra, S.; Bhosale, S. S.; Kharade, A. K.; Chang, S.; Diau, E. W.-G. Retarded Charge Recombination to Enhance Photocatalytic Performance for Water-Free CO2 Reduction Using Perovskite Nanocrystals as Photocatalysts. *J. Phys. Chem. Lett.* **2022**, *13* (39), 9134–9139.
- (50) Kaur, A.; Goswami, T.; Babu, K. J.; Ghosh, H. N. Ultrafast Hole Migration at the p-n Heterojunction of One-Dimensional SnS Nanorods and Zero-Dimensional CdS Quantum Dots. *J. Phys. Chem. Lett.* **2023**, *14* (33), 7483–7489.
- (51) Wang, S.-Y.; Zhen, X.-J.; Feng, Z.-Z.; Xiao, M.-J.; Li, S.-J.; Shang, W.; Huang, Y.-F.; Wang, Q.; Zhang, H.-L. Third-Order Optical Nonlinearities of Two-Dimensional SnS under Irradiation: Implications for Space Use. *J. Mater. Chem. C* **2022**, *10* (47), 18025–18032
- (52) Xiao, G.; Wang, X.; Li, D.; Fu, X. InVO4-Sensitized TiO2 Photocatalysts for Efficient Air Purification with Visible Light. *J. Photochem. Photobiol.*, A 2008, 193 (2–3), 213–221.
- (53) Chang, J.; Zhang, W.; Zhao, W.; Jiang, L.; Wang, G.; Ang, Y. A. Perovskite-Based SnS/CsPbBr<sub>3</sub> Heterostructure Used for Superior Optical Absorption. *Soc. Sci. Res. Netw.* **2022**, 9.

